Determination of optimal parameters for 3D single-point macromolecular proton fraction mapping at 7T in healthy and demyelinated mouse brain

Lucas Soustelle, Maria Cristina Antal, Julien Lamy, Laura-adela Harsan, Paulo Loureiro de Sousa

Determination of Optimal Parameters for 3D Single-Point Macromolecular Proton Fraction Mapping at 7T in Healthy and Demyelinated Mouse Brain

Lucas Soustelle[1,2], Maria Cristina Antal[1], Julien Lamy[1], Laura Harsan[1], Paulo Loureiro de Sousa[1]

1. **Université de Strasbourg, CNRS, ICube, Strasbourg, France**
2. **Aix-Marseille Univ, CNRS, CRMBM, Marseille, France**

Corresponding author: L. Soustelle (lucas.soustelle@univ-amu.fr), Aix-Marseille Univ., CNRS, CRMBM UMR 7339, 27 bd Jean Moulin, Faculté de Médecine, 13005, Marseille, France

Abstract

Purpose

To determine optimal constrained tissue parameters and off-resonance sequence parameters for single-point macromolecular proton fraction (SP-MPF) mapping based on a comprehensive quantitative magnetization transfer (qMT) protocol in healthy and demyelinated living mice at 7T.

Methods

Using 3D spoiled gradient echo-based sequences, a comprehensive qMT protocol is performed by sampling the Z-spectrum of mice brains, in vivo. Provided additional T_1, B_1^+ and B_0 maps allow for the estimation of qMT tissue parameters, among which three will be constrained, namely the longitudinal and transverse relaxation characteristics of the free pool ($R_{1,f}T_{2,f}$), the cross-relaxation rate (R) and the bound pool transverse relaxation time ($T_{2,r}$). Different sets of constrained parameters are investigated to reduce the bias between the SP-MPF and its reference based on the comprehensive protocol.

Results

Based on a whole-brain histograms analysis about the constrained parameters, the optimal experimental parameters that minimize the global bias between reference and SP-MPF maps consist of a 600° and 6 kHz off-resonance irradiation pulse. Following a Bland-Altman analysis over regions of interest, optimal constrained parameters were $R_{1,f}T_{2,f}$=0.0129, R=26.5 s^{-1} and $T_{2,r}$=9.1 µs, yielding an overall MPF bias of 10^{-4} (limits of agreement [-0.0068;0.0070]) and a relative variation of 0.64±5.95% between the reference and the optimal single-point method across all mice.

Conclusion

The necessity of estimating animal model- and field-dependent constrained parameters was demonstrated. The single-point MPF method can be reliably applied at 7T, as part of routine preclinical in vivo imaging protocol in mice.

Keywords: quantitative magnetization transfer; macromolecular proton fraction mapping; preclinical; mouse; myelin; cuprizone

Introduction

Quantitative magnetization transfer (qMT) imaging yields indices describing the interactions between free (water) and restricted (macromolecular) protons (1,2). These indices include the macromolecular protons fraction (MPF), which demonstrated strong interests for brain tissue characterization in healthy and pathological conditions (3–8). Sampling the Z-spectrum to derive quantitative MT parameters is time consuming because different MT-weighted (MTw) images must be acquired with a set of MT saturation pulses differing in power and off-resonance frequency. Thus, few studies reported on comprehensive qMT protocols at a whole-brain scale in living animals (9,10), 2D (11,12) and ex vivo (13–17) explorations being preferred.

Methods to reduce the number of MTw images for 3D-MPF mapping were proposed at 1.5T (humans only) (18), 3T (humans and rodents) (10,18–22) and 11.7T (rodents only) (9,23). Notably, Yarnykh's single-point MPF (SP-MPF) (9,20,21,23,24) method estimates the MPF by constraining the values of other two-pool model parameters, namely the fast cross-relaxation rate constant (R), the T_2 of the restricted pool ($T_{2,r}$), and the product of the relaxation quantities $R_{1,f}$ and $T_{2,f}$ of the free pool ($R_{1,f}T_{2,f}$) using steady-state and MT-prepared spoiled gradient echo sequences, hence using a single MTw image. The method is therefore highly interesting for fast MPF mapping.

Integrating MPF mapping as part of routine multi-modal imaging protocols in preclinical investigations would be of great value for a comprehensive insight into tissue microstructural features. When paired with diffusion tensor imaging for instance, advanced contrasts can be derived such as g-ratio mapping (25), critically important for brain white matter characterization. Demyelination and remyelination processes can potentially be assessed in longitudinal animal studies (26,27) for quantitative follow-up of therapeutic strategies effects (28,29).

While the MPF metric is conceptualized to be independent of the static field intensity, other parameters from the two-pool model such as $R_{1,f}$ and $T_{2,f}$ are not, requiring their estimation to properly tune the single-point qMT method. In this study we provide an optimized protocol and qMT parameters constraints for robust SP-MPF mapping at 7T based on a comprehensive 3D qMT imaging protocol in healthy and demyelinated living mice.

Methods

Experiments were conducted on a 7T preclinical scanner (Bruker BioSpec 70/30, Ettlingen, Germany), using an 86-mm volume transmitter coil and a mouse head surface receiver coil. Male C57BL/6 mice (3 healthy vs. 3 demyelinated with a respective mean weight of 28.1±2.1 g and 23.2±0.9 g) were scanned at 16 weeks of age. Demyelination was induced by cuprizone administration in standard chow (0.2 %) for 8 consecutive weeks prior to scanning (30). During scans under isoflurane anesthesia (2%, 0.5 L/min O_2), animal respiratory rate and temperature were monitored and maintained at 100±10 breaths-per-minute and 37.6±0.1°C. Animal studies were conducted in agreement with the European Council Directive 2010/63/EU and the French Guidelines for Animal Care from the French Department of Agriculture (Animal Rights Division) and approved by our institutional committee on ethics in animal research (CREMEAS AL/41/48/02/13).

The protocol comprised 3D spoiled gradient-echo (SPGR) based sequences: i) T_1-mapping using the Variable Flip-Angle method (VFA-SPGR), and ii) Z-spectra sampling using MT-prepared SPGR (MT-SPGR) sequences. 3D B_1^+ mapping was also performed following the Actual Flip Angle (31,32) method (AFI-SPGR) to correct deviations in T_1 and qMT estimations, as well as B_0 mapping for shim calculation and further static-field inhomogeneities compensation in qMT. Relevant parameters were: 1) VFA-SPGR: matrix size=150x140x60, voxel size=100x100x500 µm^3, TR/TE=30/2 ms, readout flip angles (FA)=6/10/30/50°, receiver bandwidth (rBW)=75 kHz (T_{acq}=4.1 min per data point); 2) MT-SPGR: matrix size=150x140x60, voxel size=100x100x500 µm^3, TR/TE=30/2 ms, FA=10°, rBW=75 kHz, 10.25-ms gaussian saturation pulse (provided by the constructor, with an actual bandwidth of 218 Hz), saturation flip angle (α_{sat})=600/800/1000° ($B_{1,peak}$=9.1/12.2/15.2 µT and $B_{1,RMS}$=5.0/6.6/8.3 µT, respectively), offset frequency of the saturation pulse (Δ)=1/2/4/6/8/20 kHz, and two additional Z-points at Δ=30/40 kHz and α_{sat}=1000° (T_{acq} =4.1 min per data point); 3) AFI-SPGR: matrix size=70x70x60, voxel size=214x214x500 µm^3, TR_1/TR_2/TE=15/60/2 ms, FA=60°, rBW=59 kHz (T_{acq}=4.0 min); 4) B_0 (dual-echo SPGR): matrix size=100x100x60, voxel size=200x200x500 µm^3, TR⁄TE_1⁄TE_2=20⁄1.65⁄3.55 ms, FA=30°, rBW=119 kHz, acquired at the protocol start; B_0 frequency adjustments were performed three times during the MT-SPGR protocol to compensate potential B_0-related drift (T_{acq} =2.0 min). To mitigate any T_1-related temperature effect throughout the protocol, the MT-SPGR

and VFA-SPGR sequences were interleaved and ordered randomly, conserving an identical order for all animals.

A strong gradient spoiling was systematically included after readouts in MT/VFA-SPGR (moment of 2317 mT/m.ms for both) and AFI-SPGR (moments of 1854 and 7414 mT/m.ms in TR_1 and TR_2, respectively) to maximize the remaining transverse magnetization crushing through diffusion effects, along with an appropriate RF spoiling increment (phase increment of 50° for VFA-SPGR and MT-SPGR, and 129° for AFI-SPGR) (32,33).

Fields of view (FOV) were tilted so that their respective edge was parallel to the corpus callosum along the genu-splenium line determined on a 2D T_2-weighted sagittal scan, thus mitigating potential partial volume effects (14).

All native images were denoised using BM4D (34) (exemplified in Figure S1) and rigidly registered onto the 10-degrees volume of the T_1 mapping protocol using ANTs (35). Brain extraction was manually performed using ITK-SNAP (36). T_1 maps were estimated using an in-house implementation (Matlab R2017b, The Mathworks Inc. Natick, MA, USA), and qMT-derived maps ($T_{2,f}$, $T_{2,r}$, MPF and R) were estimated using Yarnykh's two-pool model (37) implemented in the qMTLab toolbox (38), with $R_1=1/T_1=R_{1,r}=R_{1,f}$ (20). The slow cross-relaxation term k defined as $k=R\cdot MPF/(1-MPF)$ was also computed.

MPF maps for each animal were reconstructed by the single-point method for each combination of saturation pulse frequency offset Δ and flip angle α_{sat}, with constrained parameters based on whole-brain histograms of both groups. While Yarnykh's original method employed the median of these histograms in the human brain (presenting a 35/65% WM/GM proportion (39)), we explored the accuracy of several constrained parameter sets to be consistent with the WM/GM proportion in the mouse brain (10/90% (40)) by selecting averaged values from both group of their respective 10^{th}, 20^{th}, 30^{th}, 40^{th} and 50^{th} percentiles. The five series of reconstruction are referred hereafter to as Reconstruction #1, #2, #3, #4 and #5, respectively. Cerebro-spinal fluid was excluded from the analysis by discarding voxels with T_1 above 3000 ms (22).

The mean absolute error per voxel for each SP-MPF reconstructions was computed as (20):

$$\delta_f = \frac{1}{N}\sum_{\nu}^{N}\frac{|f_{\mathrm{ref}}(\nu) - f_{\mathrm{SP}}(\nu)|}{f_{\mathrm{ref}}(\nu)}$$

where ν is a voxel from the brain parenchyma across all mice, N the total voxels in the analysis, and f_{ref} and f_{SP} the MPF from the reference and single-point protocols, respectively.

Optimal Δ and α_{sat} were determined for the SP-MPF reconstruction #1 to #5 as the values minimizing δ_f. To evaluate the agreement between reference and SP-MPF methods within optimal experimental conditions, mean values of MPF estimated from regions of interest (ROI) comprising the somato-sensory cortex, the corpus callosum, the internal capsules and the thalamus were plotted against each other. Additionally, a ROI-based Bland-Altman analysis was performed using the same regions to estimate the bias between reference and SP-MPF values. Relative variations of SP-MPF to the reference MPF were also reported over the same regions of interest. ROIs were drawn by one of the authors (MCA, expert in mouse histology) on the reference MPF maps according to the Allen Mouse Brain Atlas (available from: http://atlas.brain-map.org/). Distributions of the difference between reference and generated SP-MPF were tested for normality using Shapiro-Wilk tests, and one-sample Student's t-tests were employed to determine whether these distributions were zero-centered.

Results

Histograms of $R_{1,f}T_{2,f}$, $T_{2,r}$, R and MPF parameters from both mice groups are shown in Figure 1, and region-averaged metrics across mice in each group are provided in Table 1. Although $R_{1,f}T_{2,f}$ is rather stable between the two groups, R, $T_{2,r}$ and MPF distributions are modified by the global brain changes induced by cuprizone diet (30). Groupwise and averaged R_1, $T_{2,r}$, $T_{2,f}$, k and MPF values estimated from the selected ROIs are summed up in Table 2. Given the estimated parameters, a sensitivity analysis about the normalized magnetization (20) is provided in Supporting Information (Figure S2).

The minimum global deviation between reference MPF and SP-MPF was reached at Δ=6 kHz and α_{sat}=600° with δ_f=8.4 %, δ_f=7.6 %, δ_f=7.4 %, δ_f=7.4 % and δ_f=7.5 % for reconstructions #1

to #5, respectively. Figure S3 in Supporting Information reports the behavior of δ_f to α_{sat} and Δ across all reconstructions.

The reference MPF values and those estimated using SP-MPF for all reconstructions were found to agree, as reported in Figure 2, with coefficients of determination $R^2>0.96$ and non-significant intercepts of the regression line ($p>0.024$). The effect of the various constrained parameters qualitatively shifted MPF values from the SP-qMT technique towards higher values with respect to Reconstruction #5 to #1. All distributions of the difference between reference and SP-MPF were considered normal following Shapiro-Wilk tests ($p>0.18$). The Bland-Altman analysis (Figure 2 and Table 1) revealed that Reconstruction #2 presented the lowest bias compared to the reference, with a zero-centered ($p=0.732$) distribution of the difference, and a relative variation of SP-MPF to reference MPF of 0.64±5.95%. Additionally, the distributions of the difference are provided in Figure 2 for separated and joint groups. Finally, the SP-MPF values across the investigated ROIs of the selected optimal reconstruction are reported in Table 2.

Figure 3 shows typical MPF maps using the comprehensive protocol and optimal reconstruction. Image differences between reference and optimal SP-MPF present localized patchy irregularities, presumably associated with low SNR scores (about 30 on the native optimal MTw) using a single MTw image for MPF computation, whereas this effect abates in the comprehensive protocol. Nonetheless, a consistent behavior can be observed with a close-to-zero difference between reference and the optimized SP-MPF.

Discussion

We demonstrated that MPF maps in mouse brain at 7T can be estimated efficiently using SP-MPF and that constrained parameters and optimal Δ and α_{sat} values must be experimentally determined for robust and accurate SP-MPF mapping. To our knowledge, the present study is the first to precisely reproduce Yarnykh's original methodology (20) applied to living mice. The optimal constrained parameters given our protocol, animal model and working field are $R_{1,f}T_{2,f}=0.0129$, $R=26.5\ s^{-1}$ and $T_{2,r}=9.1\ \mu s$, with an off-resonance saturation of 600° at 6 kHz.

Similarly to Yarnykh's original study (20), SP-MPF was assessed in healthy and pathological conditions. The demyelination model employed in the present study is widely used to mimic myelin diseases such as multiple sclerosis (30). The cuprizone diet, as applied in our experimental set-up, affects both white (acute and global demyelination of the corpus callosum observed in an 8-week diet (26)) and grey matter (41). Hence, the use of SP-MPF requires an accurate tuning of the constrained parameters by evaluating representative regions from WM and GM, both healthy and pathological. The choice of parameters remains arbitrary: Yarnykh found excellent agreement by selecting median values of each parameter from whole-brain distributions (20), whereas Naumova et al. estimated parameters at 11.7T as averaged values from selected regions of interest in in vivo healthy rat brains (9). The method has been previously investigated in other static fields and applications, but limited attention was given to these specific parameters (18,42). Although presenting the advantage of reducing the required number of images to compose MPF maps, the two-pool model remains, nonetheless, approximated. In addition, the present study as well as Yarnykh (20) and Naumova et al. (9) revealed that the constrained parameter values vary with static-field intensity and tissue model. Therefore, inherent biases and parameter constraints should be systematically identified prior to novel applications, both clinical (e.g. multiple sclerosis at high field) and preclinical (e.g. inflammatory demyelination models such as the experimental autoimmune encephalomyelitis (27)). Reconstructions of the SP-MPF maps using constrained parameters employed by Yarnykh at 3T in the human brain further emphasize this requirement (Figure S4 in Supporting Information) since a systematic MPF bias of -0.0181 (limits of agreement of -0.0263/-0.0098) is obtained between both distributions, with a relative variation between reference and SP-MPF of 28.3±5.7%. Nonetheless, the same analysis led using constrained parameters from the control group only (Reconstruction #H1 to #H5, with analyses reported in Table T1 and Figure S5 and S6 in Supporting Information) demonstrated a similar bevahior with an optimality reached for Reconstruction #H2 (i.e., parameters from the 20th percentile of the joint whole-brain distribution), with an apparent bias of 0.0004 (zero-centered; p=0.294) and slightly different limits of agreement (-0.0068/0.0070 vs. -0.0066/0.0073 in Reconstruction #2 and #H2, respectively) and relative variations (0.64±5.95% vs. 0.26±5.93% in Reconstruction #2 and #H2, respectively). Such similarity can be explained by the low discrepancy about the optimal constrained and experimental parameters (i.e. $R_{1,f}T_{2,f}$=0.0129 vs. 0.0128, R=26.5 vs. 27.1 s^{-1}, $T_{2,r}$=9.1 vs. 8.9 µs

for Reconstruction #2 vs. #H2, respectively, with common optimal α_{sat}=600° and Δ=6 kHz) and the respective limited sensitivity of the normalized magnetization (see Figure S2).

Apart from a single MT-weighted image and its paired normalizing volume, the SP-MPF composite mapping method requires prior knowledge about R_1 and system imperfections, namely B_1^+ and B_0 (24). Hence, any bias in the provided maps shall impact the resulting MPF. As B_1^+ and B_0 mapping methods are nowadays readily acquired, T_1-sensitive sequences represent the largest bias source within SPGR-based qMT protocols. This is particularly important as the MPF is significantly correlated with R_1 (13,21). For instance, incomplete magnetization spoiling will alter the predicted signals in SPGR sequences (43), deviating from ideality. Animal temperature is another critical parameter. During anesthesia induction and animal conditioning for MRI, mice body temperature decreased (approximately 33 to 35 °C). Scanning was therefore performed when body temperature reached 37.6°C. Preliminary results emphasized the temperature dependency of the comprehensive qMT protocol, leading to incoherent results due to body temperature adjustment (not shown). Both concerns were addressed in the present study by employing RF spoiling in pair with large gradient spoiling, while conscientiously regulating animal temperature throughout the protocol. We therefore encourage further preclinical qMT studies to provide this information for sake of consistency across investigations.

MPF values measured in WM and GM regions in this study are in average similar to those reported by Ou et al. (17) (recalculated from the pool size ratio), Thiessen et al. (13) and by our group (14) in paraformaldehyde-fixed mouse brains. Values were somewhat lower than those estimated by Khodanovich et al. (23) in in vivo mice at 11.7T, although precise constrained parameters were not provided. Discrepancies between values found in healthy rats (9) and mice may lie in the difference of animal model as well as partial volume effect due to the high anisotropy in the slice direction.

In this study, the selected constrained $T_{2,r}$ parameter ($T_{2,r}$=9.1 µs) is seemingly lower than that used at 3T ($T_{2,r}$=9.8 µs) in the human brain (20) and at 11.7T ($T_{2,r}$=10.3 µs) in the rat brain (10) based on comprehensive protocols. Whereas $R_{1,f}T_{2,f}$ and R are rather different between grey and white matter (i.e. both lower in healthy WM than in GM) (9,12,13), this particular parameter is sensitive to the orientation of WM fibers relative to B_0 (20,44), questioning the appropriate choice for constraint. However, we evidenced a low sensitivity

(< 0.8%) of the saturated M_z quantity to $T_{2,r}$ in the qMT model given our working optimal sequence parameter (Δ=6 kHz, α_{sat}=600°; Figure S2), hence limiting potential bias due to inaccuracies about the constrained $T_{2,r}$ in the proposed framework.

Surprisingly and similarly to Yarnykh study (20), the product $R_{1,f}T_{2,f}$ was rather identically distributed in the mouse brain between healthy and demyelinated conditions, with reported mean values of 0.0172 in both groups. As a global tissue disease can be observed in the course of 8-week cuprizone diet, the decrease of R_1 due to its sensitivity to molecular content is hence balanced by an increase of estimated $T_{2,f}$. The mean and median $R_{1,f}T_{2,f}$ values estimated in the whole brain in this study are between those estimated in the human brain at 3T ($R_{1,f}T_{2,f}$=0.022) (20) and in the rat brain at 11.7T ($R_{1,f}T_{2,f}$=0.013) (9), although the constrained value in our study ($R_{1,f}T_{2,f}$=0.0129) at 7T is similar to that of the rat brain at 11.7T. Nonetheless, comparing this specific parameter on a whole-brain scale is complex since depending on the working field and tissue model.

Cross-relaxation k parameter measured in the present study (reported in Table 1) was higher in white matter than in grey matter, which is consistent with the literature (7,9,12,13,20,45,46), and dropped following cuprizone diet (13). As discussed by Naumova et al. (9), reported values from the literature are highly variable. Furthermore and to our knowledge, the sole study estimating the cross-relaxation parameters in living healthy mice was performed by Turati et al. (11), and presented rather low values in the corpus callosum (estimated k of about 1.0 s^{-1}).

T_1 values in most affected tissues did not exceed values of about 2200 ms (e.g. corpus callosum in the cuprizone group with mean R_1=0.46 s^{-1}). In this study, we excluded CSF voxels defined by T_1>3000 ms in order to focus the whole-brain analysis on the brain parenchyma. This assumption may however include voxels close to ventricles due to partial volume effect (e.g. corpus callosum), and a 3-pool qMT model may be more appropriate to properly segment the brain parenchyma based on relevant qMT parameters (47). Nonetheless, the remaining number of voxels involved in the analyses was considered large enough (about 100,000 per group) to accurately sustain the global analysis for parameter constraints.

The original SP-MPF method requires providing both R_1 and B_1^+ information. Although attention was given to potential insufficient spoiling in the respective VFA-SPGR and AFI-SPGR protocols, both methods are known to be sensitive to magnetization transfer effects (48–50), further biasing these priors. Mossahebi et al. evidenced the bias of the qMT estimators between cases where $R_{1,f}$ is provided as a prior (i.e. computed while neglecting MT effects) and integrated in the qMT two-pool model to account for MT effects in VFA-SPGR protocols (51). Henceforth, a qMT model including a joint estimation of qMT parameters, VFA-based $R_{1,f}$ and AFI-based B_1^+ is seemingly more appropriate.

The resultant conclusion from preclinical studies is that qMT tissue parameters depend on many experimental aspects, such as animal model (17), temperature (52), static field intensity, B_0 and B_1^+ inhomogeneities, tissue fixation conditions (13), qMT model (53) and T_1 mapping methods sensitive to incomplete spoiling (33,43). As such, efforts should be made to establish consensus about optimal comprehensive qMT protocol necessary for the quantification of qMT parameters, which remains essential for single-point MPF mapping implementation.

Conclusion

We established optimal parameters for single-point MPF mapping for in vivo healthy and demyelinated mice at 7T, with an optimality criterion minimizing the bias in regions of interest between a reference MPF maps generated via a full Z-spectrum analysis and the fast MPF maps. Estimating these animal model- and field-dependent parameters appears essential since a large bias was found with regard to the reference MPF when using constrained parameters optimized at 3T in the human brain. This allows for the integration of an MPF mapping methodology in multi-modal in vivo imaging protocols by reducing the total acquisition duration to about 20 minutes given the proposed geometry in a whole-brain study. More sensitive signal reception systems may further allow increasing voxel resolution within identical scan time by taking advantage of partial Fourier sampling given the SNR boost.

Figures caption

Figure 1: Normalized histograms of Control (CTL; dark line) and Cuprizone (CPZ; grey line) mice corresponding to the distributions of $R_{1,f}T_{2,f}$ (a; bin size = 0.00022), R (b; bin size = 0.5 s^{-1}), $T_{2,r}$ (c; bin size = 0.12 µs) and MPF (d; bin size = 0.0006).

Figure 2: Comparison of averaged MPF values from averaged ROIs across all mice between reference (f_{ref}) and optimized SP-MPF (left column) and corresponding Bland-Altman plots from slice-wise averaged ROIs (middle column), and respective density distributions of the difference of each and joint groups (right column) for reconstructions #1 (a-c), #2 (d-f), #3 (g-i), #4 (g-l) and #5 (m-o). The solid line on left-sided plots corresponds to the line of unity, indicating the deviation of the SP-MPF reconstruction from ideality. Solid lines and dashed lines on Bland-Altman plots depict the mean and the limits of agreement (defined as mean±1.96 x standard deviation) of the distribution of the differences, respectively. Plotted ROIs are represented by the somato-sensory cortex (crosses), corpus callosum (bullets), internal capsules (diamonds) and thalamus (plus signs). Control and cuprizone mice are depicted, if appropriate, in black and grey ticks, respectively.

Figure 3: Representative axial views of reference and SP-qMT MPF maps and corresponding image differences of a typical mouse from the Control (upper part) and Cuprizone (lower part) groups. Slices were selected about the bregma at 0.15 mm (left column), -0.85 mm (middle column) and -1.85 mm (right column).

Supporting Information

Additional Supporting Information may be found in the online version of this article.

Figure S1: Exemplification of native weighted images denoising using BM4D from the Variable Flip Angle (VFA) and Magnetization Transfer (MTw) protocols.

Figure S2: Sensitivity analysis of normalized MT signal (mz) in the Corpus Callosum (CC; a-b), Somato-Sensory Cortex (CTX; c-d) and affected Corpus Callosum (CCCPZ; e-f) as a function of Δ (fixed α_{sat} of 600°; left column) and αsat (fixed Δ of 6 kHz; right column) and about qMT parameters (p): $T_{2,r}$ (green), $T_{2,f}$ (blue), f (black) and R (red). Respective fixed parameters can be found in Table 2: CC: R_1=0.55 s^{-1}, f=0.087, R=24.1 s^{-1}, $T_{2,f}$=23.1 ms and $T_{2,r}$=10.6 µs; CTX: R_1=0.48 s^{-1}, f=0.058, R=32.5 s^{-1}, $T_{2,f}$=30.4 ms and $T_{2,r}$=9.8 µs; CCCPZ: R_1=0.46 s^{-1}, f=0.049, R=31.1 s^{-1}, $T_{2,f}$=32.4 ms and $T_{2,r}$=9.9 µs. Black dashed vertical lines indicate optimal working experimental parameters (i.e., Δ=6 kHz and α_{sat}=600°). Other sequence parameters are detailed in the Methods section. Reported S_p values were computed as the average sensitivity value over a range of p spanning over acceptable values from the whole brain respective distributions (i.e., $T_{2,r}$=[7.0;14.0] µs, f=[0.03;0.10], R=[5;60] s^{-1}, $R_{1,f}T_{2,f}$=[0.01;0.03] ms).

Similarly to Yarnykh's original study, and within the considered experimental and optimized protocol, the highest sensitivity in all three structures is related to f (S_p>24.8%), and remain systematically superior to that of R (S_p<9.8%), $T_{2,f}$ (S_p<4%) and $T_{2,r}$ (S_p<0.8%). These results emphasize the feasibility of single-point MPF estimation.

Figure S3: Mean errors on δ_f averaged across all mice using Reconstruction #1 (a), Reconstruction #2 (b), Reconstruction #3 (c), Reconstruction #4 (d) and Reconstruction #5 (e) along α_{sat} and Δ.

Figure S4: Comparison of averaged MPF values from averaged ROIs across all mice between reference (f_{ref}) and SP-MPF ($f_{600°/4\ kHz}$) using optimized 3T constrained parameters in the human brain from (R=19.0 s^{-1}, $R_{1,f}T_{2,f}$=0.022 and $T_{2,r}$=9.7 µs; Δ=4 kHz and α_{sat}=600°), yielding an overestimation of SP-MPF values (a). Distribution of the difference between both estimated MPF in the various regions (crosses: somato-sensory cortex; bullets: corpus callosum; diamonds: internal capsules; plus signs: thalamus) from both groups (black:

control; grey: cuprizone) yielded an MPF bias of -0.0181 (limits of agreement=-0.0263/-0.0098) following a Bland-Altman analysis (b). Density of the distributions of the difference are also reported (c). The relative variation between reference MPF and SP-MPF over the ROIs used in the Bland-Altman analysis amounted to 28.3±5.7%.

Table T1: Summary of constrained parameters $R_{1,f}T_{2,f}$, R and $T_{2,r}$ from the whole-brain histogram analysis on the healthy mice group, and used in SP-MPF reconstruction #H1 to #H5. Biases and limits of agreement (defined as mean±1.96 x standard deviation) over joint groups from the Bland-Altman analysis and statistics of the relative variation between reference MPF and SP-MPF are also presented, as well as one sample t-test testing whether the MPF distributions between reference and SP-qMT (all presenting a normal behavior; $p>0.14$) from the corresponding reconstruction were zero-centered. Estimated Pearson correlations between reference and single-point MPF were systematically significantly high ($R^2>0.96$; $p<0.001$), with non-significant intercept of the regression line ($p>0.01$).

Figure S5: Mean errors on δ_f averaged across all mice using Reconstruction #H1 (a), Reconstruction #H2 (b), Reconstruction #H3 (c), Reconstruction #H4 (d) and Reconstruction #H5 (e) along α_{sat} and Δ. Parameters of the different reconstruction schemes are reported in Table T1. Similarly to the main analysis, optimal experimental parameters yielding the lowest δ_f values are systematically reached at α_{sat}=600° and Δ=6 kHz.

Figure S6: Comparison of averaged MPF values from averaged ROIs across all mice between reference (f_{ref}) and optimized SP-MPF (left column) and corresponding Bland-Altman plots from slice-wise averaged ROIs (middle column), and respective normalized density distributions of the difference of each and joint groups (right column) for reconstructions #H1 (a-c), #H2 (d-f), #H3 (g-i), #H4 (g-l) and #H5 (m-o). Optimized parameters from SP-MPF estimations were taken from the control group only (see values in Table T1). The solid line on left-sided plots corresponds to the line of unity, indicating the deviation of the SP-MPF reconstruction from ideality. Solid lines and dashed lines on Bland-Altman plots depict the mean and the limits of agreement (defined as mean±1.96 x standard deviation) of the distribution of the differences, respectively. Plotted ROIs are represented by the somato-sensory cortex (crosses), corpus callosum (bullets), internal capsules (diamonds) and thalamus (plus signs). Control and cuprizone mice are depicted, if appropriate, in black and grey ticks, respectively.

Table 1: Summary of constrained parameters $R_{1,f}T_{2,f}$, R and $T_{2,r}$ from the whole-brain histogram analysis, and used in reconstruction #1 to #5 (represented as Averaged (Control/Cuprizone)). Biases and limits of agreement (defined as mean±1.96 x standard deviation) from the Bland-Altman analysis and statistics of the relative variation between reference MPF and SP-MPF are also presented, as well as one sample t-test testing whether the MPF distributions between reference and SP-qMT from the corresponding reconstruction were zero-centered.

		$R_{1,f}T_{2,f}$	R (s^{-1})	$T_{2,r}$ (µs)	MPF Bias (Limits of agreement)	MPF Relative variation (mean±std)	One sample t-test	Intercept f_{ref} vs. $f_{600°/6\ kHz}$
Reconstruction	#1	0.0119 (0.0118/0.0120)	22.9 (22.7/23.1)	8.8 (8.6/9.0)	-0.0013 (-0.0079/0.0054)	2.79±6.07%	H=1 (p<0.001)	-0.0069 (p=0.030)
	#2	0.0129 (0.0128/0.0130)	26.5 (27.1/25.9)	9.1 (8.9/9.4)	0.0001 (-0.0068/0.0070)	0.64±5.95%	**H=0 (p=0.732)**	-0.0071 (p=0.028)
	#3	0.0136 (0.0136/0.0136)	28.7 (29.7/27.6)	9.4 (9.1/9.6)	0.0009 (-0.0062/0.0080)	-0.53±5.89%	H=1 (p=0.015)	-0.0072 (p=0.026)
	#4	0.0142 (0.0142/0.0142)	30.4 (31.7/29.1)	9.6 (9.3/9.8)	0.0014 (-0.0058/0.0086)	-1.34±5.85%	H=1 (p<0.001)	-0.0073 (p=0.025)
	#5	0.0148 (0.0148/0.0148)	31.9 (33.5/30.4)	9.8 (9.5/10.0)	0.0018 (-0.0055/0.0091)	-1.98±5.81%	H=1 (p<0.001)	-0.0075 (p=0.024)

Table 2: Summary of the relaxation, cross-relaxation and MPF parameters of selected regions in the healthy (CTL) and pathological (CPZ) mouse brain at 7T in the Corpus Callosum (CC), Internal Capsules (IC), Somato-sensory Cortex (SSC) and Thalamus (Th). Means and standard deviations were computed from the joint voxel distributions of the respective ROIs of each mice group. MPF from the optimized single-point reconstruction #2 is reported (SP-MPF).

	Region	R_1 (s^{-1})	k (s^{-1})	$T_{2,f}$ (ms)	$T_{2,r}$ (µs)	MPF	SP-MPF
CTL	CC	0.55 ± 0.03	2.3 ± 0.3	23.1 ± 3.5	10.6 ± 0.8	0.087 ± 0.010	0.084 ± 0.010
	IC	0.58 ± 0.03	2.5 ± 0.3	24.6 ± 4.7	11.9 ± 1.1	0.092 ± 0.011	0.089 ± 0.010
	SSC	0.48 ± 0.01	2.0 ± 0.1	30.4 ± 3.6	9.8 ± 0.5	0.058 ± 0.003	0.058 ± 0.003
	Th	0.53 ± 0.03	2.3 ± 0.2	27.5 ± 2.5	10.3 ± 0.8	0.070 ± 0.006	0.071 ± 0.006
CPZ	CC	0.46 ± 0.03	1.6 ± 0.3	32.4 ± 6.6	9.9 ± 0.9	0.049 ± 0.006	0.050 ± 0.007
	IC	0.55 ± 0.05	2.1 ± 0.3	28.9 ± 4.6	11.5 ± 1.0	0.069 ± 0.010	0.069 ± 0.009
	SSC	0.46 ± 0.03	1.8 ± 0.2	29.7 ± 3.1	9.3 ± 0.6	0.049 ± 0.004	0.052 ± 0.006
	Th	0.49 ± 0.03	1.9 ± 0.3	30.3 ± 2.1	9.6 ± 0.8	0.054 ± 0.004	0.055 ± 0.006

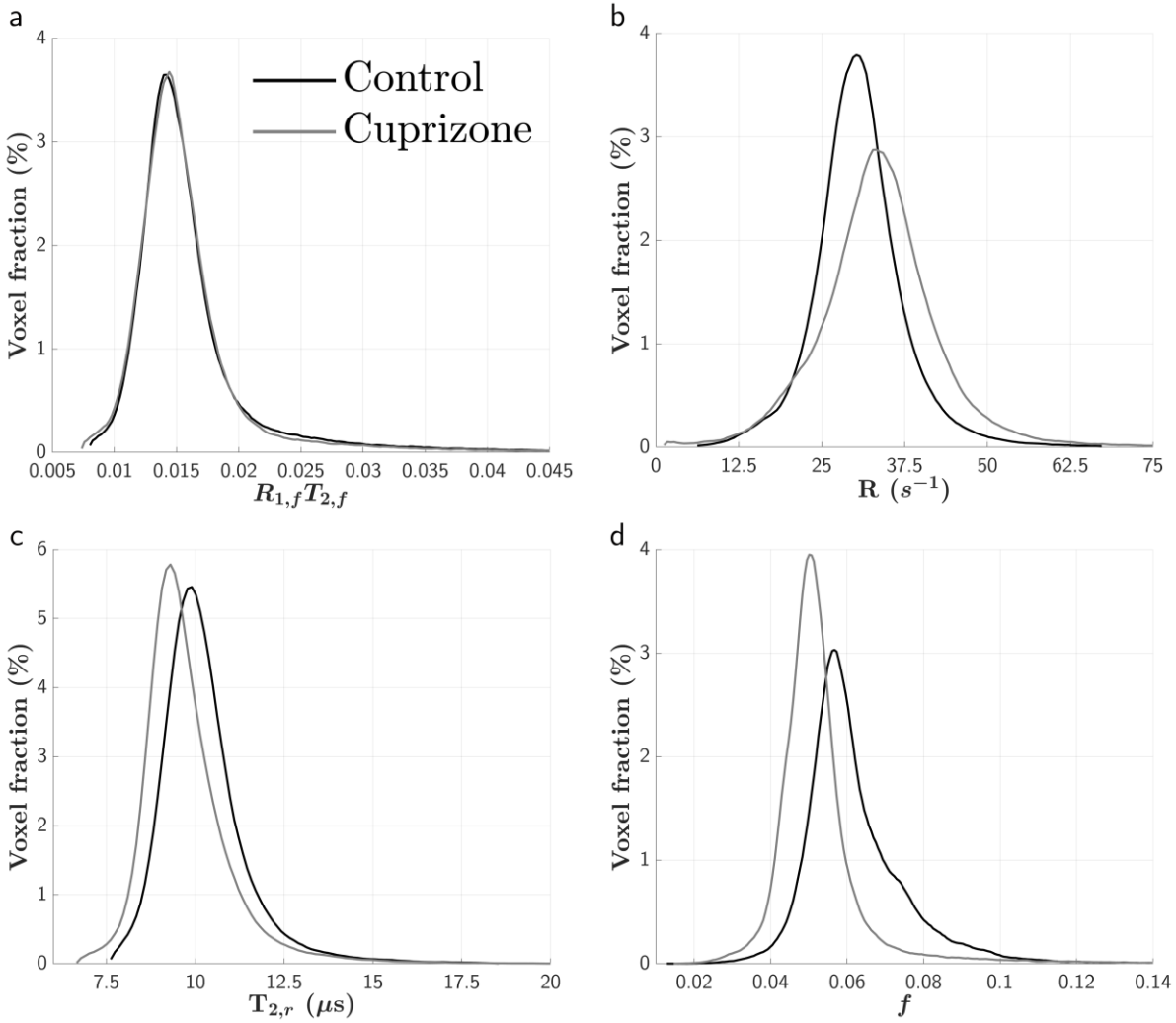

Figure 1: Normalized histograms of Control (CTL; dark line) and Cuprizone (CPZ; grey line) mice corresponding to the distributions of $R_{1,f}T_{2,f}$ (a; bin size = 0.00022), R (b; bin size = 0.5 s^{-1}), $T_{2,r}$ (c; bin size = 0.12 µs) and MPF (d; bin size = 0.0006).

Figure 2: Comparison of averaged MPF values from averaged ROIs across all mice between reference (f_{ref}) and optimized SP-MPF (left column) and corresponding Bland-Altman plots from slice-wise averaged ROIs (middle column), and respective density distributions of the difference of each and joint groups (right column) for reconstructions #1 (a-c), #2 (d-f), #3 (g-i), #4 (g-l) and #5 (m-o). The solid line on left-sided plots corresponds to the line of unity, indicating the deviation of the SP-MPF reconstruction from ideality. Solid lines and dashed lines on Bland-Altman plots depict the mean and the limits of agreement (defined as mean±1.96 x standard deviation) of the distribution of the differences, respectively. Plotted ROIs are represented by the somato-sensory cortex (crosses), corpus callosum (bullets), internal capsules (diamonds) and thalamus (plus signs). Control and cuprizone mice are depicted, if appropriate, in black and grey ticks, respectively.

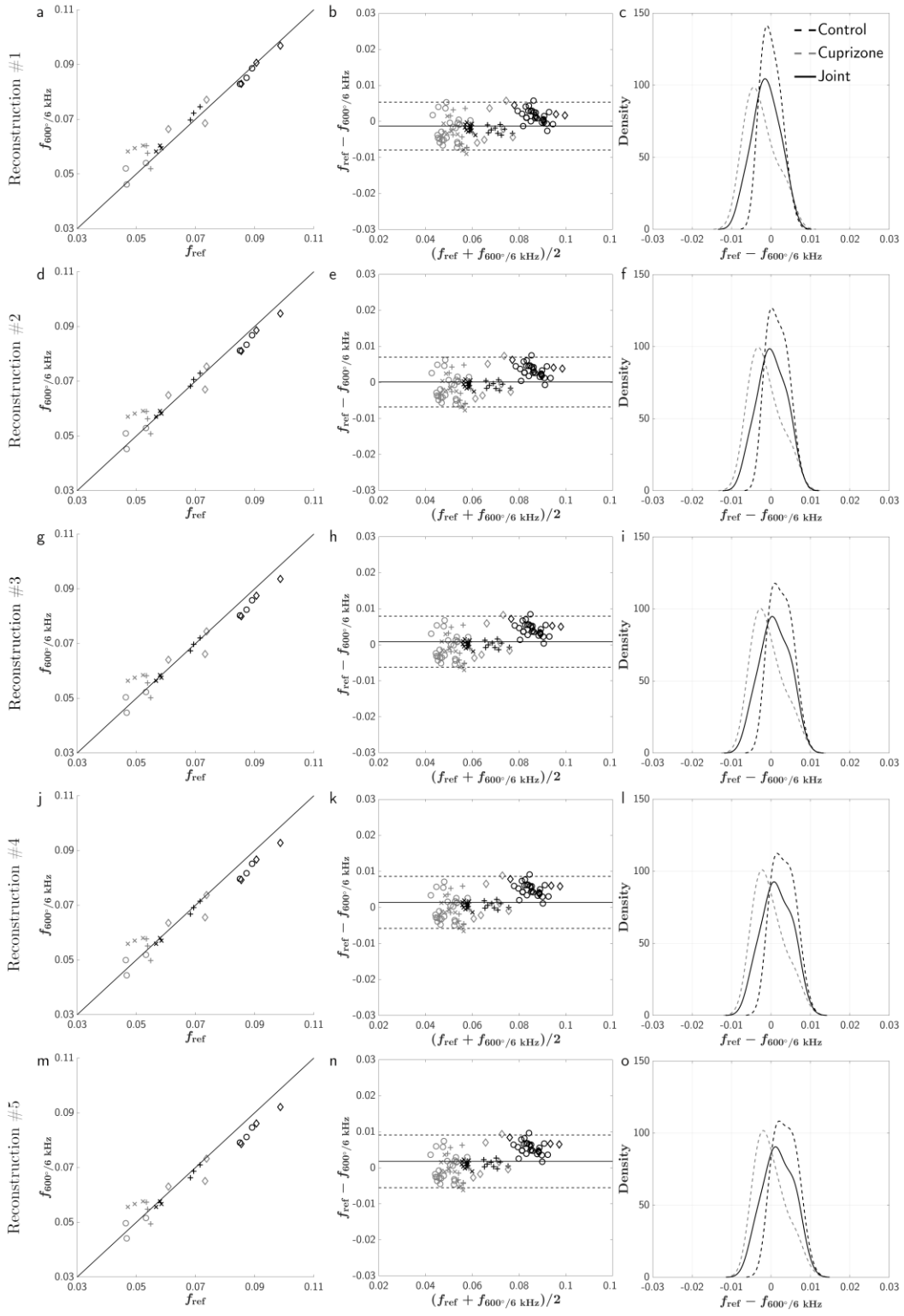

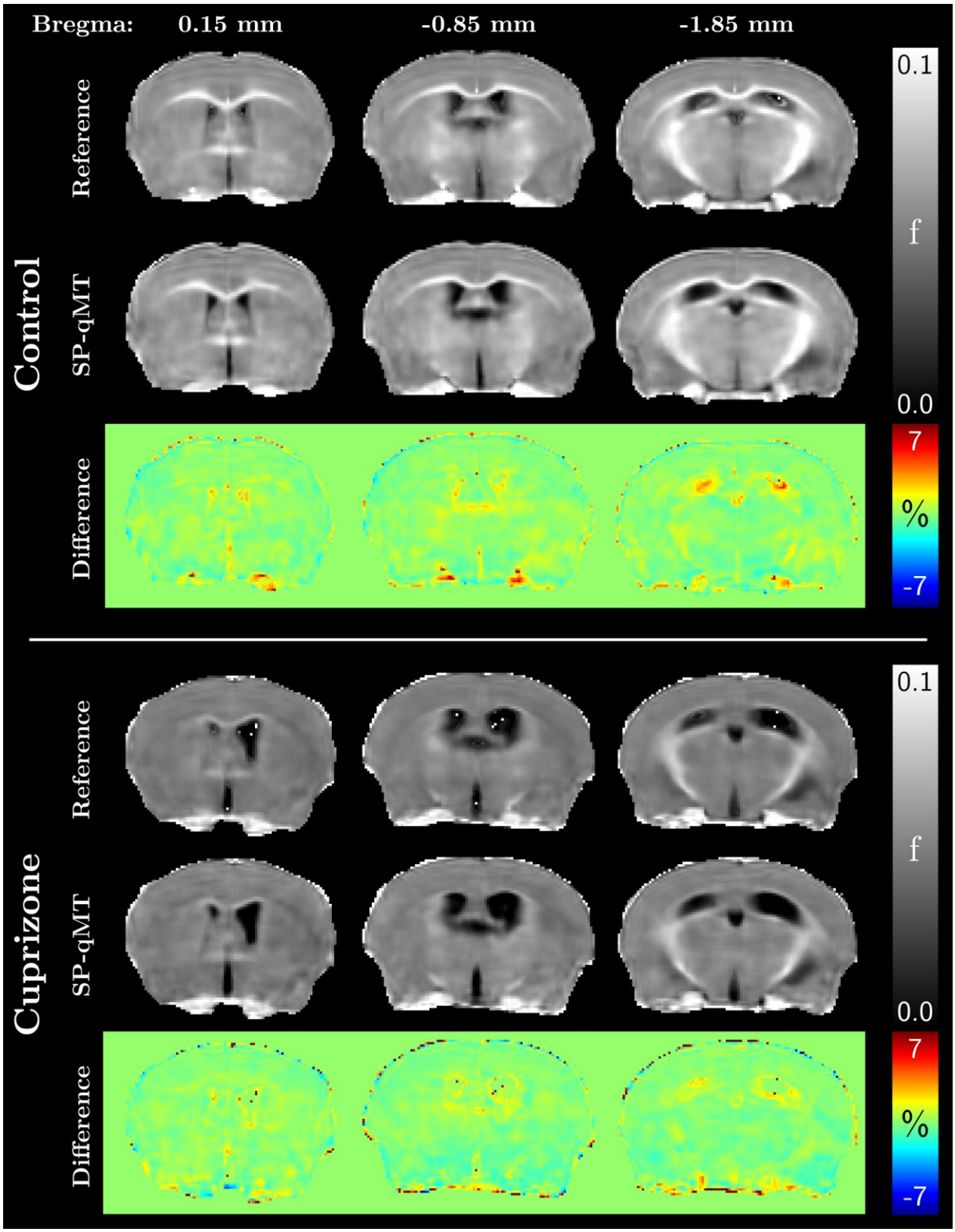

Figure 3: Representative axial views of reference and SP-qMT MPF maps and corresponding image differences of a typical mouse from the Control (upper part) and Cuprizone (lower part) groups. Slices were selected about the bregma at 0.15 mm (left column), -0.85 mm (middle column) and -1.85 mm (right column).

1. Morrison C, Henkelman RM. A Model for Magnetization Transfer in Tissues. Magn. Reson. Med. 1995;33:475–482 doi: 10.1002/mrm.1910330404.

2. Henkelman RM, Huang X, Xiang Q-S, Stanisz GJ, Swanson SD, Bronskill MJ. Quantitative interpretation of magnetization transfer. Magn. Reson. Med. 1993;29:759–766 doi: 10.1002/mrm.1910290607.

3. Tozer D, Ramani A, Barker GJ, Davies GR, Miller DH, Tofts PS. Quantitative magnetization transfer mapping of bound protons in multiple sclerosis. Magn. Reson. Med. 2003;50:83–91 doi: 10.1002/mrm.10514.

4. Davies G, Tozer D, Cercignani M, et al. Estimation of the macromolecular proton fraction and bound pool T2 in multiple sclerosis. Mult. Scler. J. 2004;10:607–613 doi: 10.1191/1352458504ms1105oa.

5. Sled JG, Levesque I, Santos AC, et al. Regional variations in normal brain shown by quantitative magnetization transfer imaging. Magn. Reson. Med. 2004;51:299–303 doi: 10.1002/mrm.10701.

6. Foucher JR, Mainberger O, Lamy J, et al. Multi-parametric quantitative MRI reveals three different white matter subtypes Gu Q, editor. PLoS One 2018;13:e0196297 doi: 10.1371/journal.pone.0196297.

7. Samsonov A, Alexander AL, Mossahebi P, Wu Y-C, Duncan ID, Field AS. Quantitative MR imaging of two-pool magnetization transfer model parameters in myelin mutant shaking pup. Neuroimage 2012;62:1390–1398 doi: 10.1016/j.neuroimage.2012.05.077.

8. Schmierer K, Wheeler-Kingshott CAM, Tozer DJ, et al. Quantitative magnetic resonance of postmortem multiple sclerosis brain before and after fixation. Magn. Reson. Med. 2008;59:268–277 doi: 10.1002/mrm.21487.

9. Naumova A V., Akulov AE, Khodanovich MY, Yarnykh VL. High-resolution three-dimensional macromolecular proton fraction mapping for quantitative neuroanatomical imaging of the rodent brain in ultra-high magnetic fields. Neuroimage 2017;147:985–993 doi: 10.1016/j.neuroimage.2016.09.036.

10. Underhill HR, Rostomily RC, Mikheev AM, Yuan C, Yarnykh VL. Fast bound pool fraction imaging of the in vivo rat brain: Association with myelin content and validation in the C6 glioma model. Neuroimage 2011;54:2052–2065 doi: 10.1016/j.neuroimage.2010.10.065.

11. Turati L, Moscatelli M, Mastropietro A, et al. In vivo quantitative magnetization transfer imaging correlates with histology during de- and remyelination in cuprizone-treated mice. NMR Biomed. 2015;28:327–337 doi: 10.1002/nbm.3253.

12. Pohmann R, Shajan G, Balla DZ. Contrast at high field: Relaxation times, magnetization transfer and phase in the rat brain at 16.4 T. Magn. Reson. Med. 2011;66:1572–1581 doi: 10.1002/mrm.22949.

13. Thiessen JD, Zhang Y, Zhang H, et al. Quantitative MRI and ultrastructural examination of the cuprizone mouse model of demyelination. NMR Biomed. 2013;26:1562–1581 doi: 10.1002/nbm.2992.

14. Soustelle L, Antal MC, Lamy J, Rousseau F, Armspach J-P, Loureiro de Sousa P.

Correlations of quantitative MRI metrics with myelin basic protein (MBP) staining in a murine model of demyelination. NMR Biomed. 2019;32:e4116 doi: 10.1002/nbm.4116.

15. Janve V a., Zu Z, Yao SY, et al. The radial diffusivity and magnetization transfer pool size ratio are sensitive markers for demyelination in a rat model of type III multiple sclerosis (MS) lesions. Neuroimage 2013;74:298–305 doi: 10.1016/j.neuroimage.2013.02.034.

16. Ou X, Sun S-W, Liang H-F, Song S-K, Gochberg DF. Quantitative magnetization transfer measured pool-size ratio reflects optic nerve myelin content in ex vivo mice. Magn. Reson. Med. 2009;61:364–371 doi: 10.1002/mrm.21850.

17. Ou X, Sun S-W, Liang H-F, Song S-K, Gochberg DF. The MT pool size ratio and the DTI radial diffusivity may reflect the myelination in shiverer and control mice. NMR Biomed. 2009;22:480–487 doi: 10.1002/nbm.1358.

18. Yarnykh V, Korostyshevskaya A. Implementation of fast macromolecular proton fraction mapping on 1.5 and 3 Tesla clinical MRI scanners: preliminary experience. J. Phys. Conf. Ser. 2017;886:012010 doi: 10.1088/1742-6596/886/1/012010.

19. Underhill HR, Yuan C, Yarnykh VL. Direct quantitative comparison between cross-relaxation imaging and diffusion tensor imaging of the human brain at 3.0 T. Neuroimage 2009;47:1568–1578 doi: 10.1016/j.neuroimage.2009.05.075.

20. Yarnykh VL. Fast macromolecular proton fraction mapping from a single off-resonance magnetization transfer measurement. Magn. Reson. Med. 2012;68:166–178 doi: 10.1002/mrm.23224.

21. Yarnykh VL, Bowen JD, Samsonov A, et al. Fast Whole-Brain Three-dimensional Macromolecular Proton Fraction Mapping in Multiple Sclerosis. Radiology 2015;274:210–220 doi: 10.1148/radiol.14140528.

22. Yarnykh VL. Time-efficient, high-resolution, whole brain three-dimensional macromolecular proton fraction mapping. Magn. Reson. Med. 2016;75:2100–2106 doi: 10.1002/mrm.25811.

23. Khodanovich MY, Sorokina I V., Glazacheva VY, et al. Histological validation of fast macromolecular proton fraction mapping as a quantitative myelin imaging method in the cuprizone demyelination model. Sci. Rep. 2017;7:46686 doi: 10.1038/srep46686.

24. Yarnykh VL, Kisel AA, Khodanovich MY. Scan–Rescan Repeatability and Impact of B 0 and B 1 Field Nonuniformity Corrections in Single-Point Whole-Brain Macromolecular Proton Fraction Mapping. J. Magn. Reson. Imaging 2019:jmri.26998 doi: 10.1002/jmri.26998.

25. Stikov N, Perry LM, Mezer A, et al. Bound pool fractions complement diffusion measures to describe white matter micro and macrostructure. Neuroimage 2011;54:1112–21 doi: 10.1016/j.neuroimage.2010.08.068.

26. Matsushima GK, Morell P. The Neurotoxicant, Cuprizone, as a Model to Study Demyelination and Remyelination in the Central Nervous System. Brain Pathol. 2006;11:107–116 doi: 10.1111/j.1750-3639.2001.tb00385.x.

27. Constantinescu CS, Farooqi N, O'Brien K, Gran B. Experimental autoimmune encephalomyelitis (EAE) as a model for multiple sclerosis (MS). Br. J. Pharmacol.

2011;164:1079–1106 doi: 10.1111/j.1476-5381.2011.01302.x.

28. Harsan L-A, Steibel J, Zaremba A, et al. Recovery from Chronic Demyelination by Thyroid Hormone Therapy: Myelinogenesis Induction and Assessment by Diffusion Tensor Magnetic Resonance Imaging. J. Neurosci. 2008;28:14189–14201 doi: 10.1523/JNEUROSCI.4453-08.2008.

29. Magalon K, Zimmer C, Cayre M, et al. Olesoxime accelerates myelination and promotes repair in models of demyelination. Ann. Neurol. 2012;71:213–226 doi: 10.1002/ana.22593.

30. Torkildsen Ø, Brunborg LA, Myhr K-M, Bø L. The cuprizone model for demyelination. Acta Neurol. Scand. 2008;117:72–76 doi: 10.1111/j.1600-0404.2008.01036.x.

31. Yarnykh VL. Actual flip-angle imaging in the pulsed steady state: A method for rapid three-dimensional mapping of the transmitted radiofrequency field. Magn. Reson. Med. 2007;57:192–200 doi: 10.1002/mrm.21120.

32. Nehrke K. On the steady-state properties of actual flip angle imaging (AFI). Magn. Reson. Med. 2009;61:84–92 doi: 10.1002/mrm.21592.

33. Zur Y, Wood ML, Neuringer LJ. Spoiling of transverse magnetization in steady-state sequences. Magn. Reson. Med. 1991;21:251–263 doi: 10.1002/mrm.1910210210.

34. Maggioni M, Katkovnik V, Egiazarian K, Foi A. Nonlocal Transform-Domain Filter for Volumetric Data Denoising and Reconstruction. IEEE Trans. Image Process. 2013;22:119–133 doi: 10.1109/TIP.2012.2210725.

35. Avants BB, Tustison N, Song G. Advanced Normalization Tools (ANTS). Insight J. 2 2009:1–35.

36. Yushkevich PA, Piven J, Hazlett HC, et al. User-guided 3D active contour segmentation of anatomical structures: Significantly improved efficiency and reliability. Neuroimage 2006;31:1116–1128 doi: 10.1016/j.neuroimage.2006.01.015.

37. Yarnykh VL, Yuan C. Cross-relaxation imaging reveals detailed anatomy of white matter fiber tracts in the human brain. Neuroimage 2004;23:409–424 doi: 10.1016/j.neuroimage.2004.04.029.

38. Cabana J-F, Gu Y, Boudreau M, et al. Quantitative magnetization transfer imaging made easy with qMTLab : Software for data simulation, analysis, and visualization. Concepts Magn. Reson. Part A 2015;44A:263–277 doi: 10.1002/cmr.a.21357.

39. Luders E, Steinmetz H, Jancke L. Brain size and grey matter volume in the healthy human brain. Neuroreport 2002;13:2371–2374 doi: 10.1097/00001756-200212030-00040.

40. Zhang K, Sejnowski TJ. A universal scaling law between gray matter and white matter of cerebral cortex. Proc. Natl. Acad. Sci. 2000;97:5621–5626 doi: 10.1073/pnas.090504197.

41. Skripuletz T, Gudi V, Hackstette D, Stangel M. De- and remyelination in the CNS white and grey matter induced by cuprizone: The old, the new, and the unexpected. Histol. Histopathol. 2011;26:1585–1597 doi: 10.14670/HH-26.1585.

42. Yarnykh VL, Prihod'ko IY, Savelov AA, Korostyshevskaya AM. Quantitative Assessment of Normal Fetal Brain Myelination Using Fast Macromolecular Proton Fraction Mapping. Am. J.

Neuroradiol. 2018;39:1341–1348 doi: 10.3174/ajnr.A5668.

43. Preibisch C, Deichmann R. Influence of RF spoiling on the stability and accuracy of T1 mapping based on spoiled FLASH with varying flip angles. Magn. Reson. Med. 2009;61:125–135 doi: 10.1002/mrm.21776.

44. Pampel A, Müller DK, Anwander A, Marschner H, Möller HE. Orientation dependence of magnetization transfer parameters in human white matter. Neuroimage 2015;114:136–146 doi: 10.1016/j.neuroimage.2015.03.068.

45. Stanisz GJ, Odrobina EE, Pun J, et al. T1, T2 relaxation and magnetization transfer in tissue at 3T. Magn. Reson. Med. 2005;54:507–512 doi: 10.1002/mrm.20605.

46. Dortch RD, Li K, Gochberg DF, et al. Quantitative magnetization transfer imaging in human brain at 3 T via selective inversion recovery. Magn. Reson. Med. 2011;66:1346–1352 doi: 10.1002/mrm.22928.

47. Mossahebi P, Alexander AL, Field AS, Samsonov AA. Removal of cerebrospinal fluid partial volume effects in quantitative magnetization transfer imaging using a three-pool model with nonexchanging water component. Magn. Reson. Med. 2015;74:1317–1326 doi: 10.1002/mrm.25516.

48. A.G. Teixeira RP, Malik SJ, Hajnal J V. Fast quantitative MRI using controlled saturation magnetization transfer. Magn. Reson. Med. 2018:1–14 doi: 10.1002/mrm.27442.

49. A. G. Teixeira RP, Neji R, Wood TC, Baburamani AA, Malik SJ, Hajnal J V. Controlled saturation magnetization transfer for reproducible multivendor variable flip angle T 1 and T 2 mapping. Magn. Reson. Med. 2019:mrm.28109 doi: 10.1002/mrm.28109.

50. Malik SJ, Teixeira RPAG, Hajnal J V. Magnetization Transfer effects in Actual Flip angle Imaging. In: Proceedings 26th Scientific Meeting, International Society for Magnetic Resonance in Medicine. ; 2018. p. 1132.

51. Mossahebi P, Yarnykh VL, Samsonov A. Analysis and correction of biases in cross-relaxation MRI due to biexponential longitudinal relaxation. Magn. Reson. Med. 2014;71:830–838 doi: 10.1002/mrm.24677.

52. Abragam A. The Principles of Nuclear Magnetism. Press, Oxf. London; 1961.

53. Cercignani M, Barker GJ. A comparison between equations describing in vivo MT: The effects of noise and sequence parameters. J. Magn. Reson. 2008;191:171–183 doi: 10.1016/j.jmr.2007.12.012.